NUMERICAL MODEL-BASED DIAGNOSTIC STUDY OF THE RAPID DEVELOPMENT PHASE OF THE PRESIDENTS' DAY CYCLONE

Louis W. Uccellini[1], Jeffrey S. Whitaker[2],
Keith F. Brill[3], and Paul J. Kocin[1]

[1]Laboratory for Atmospheres
NASA/Goddard Space Flight Center
Greenbelt, MD 20771
USA

[2]Department of Meteorology
Florida State University
Tallahassee, FL 32306
USA

[3]General Sciences Corporation
Laurel, MD 20707
USA

1.   INTRODUCTION

In part I of this two-part paper, a series of regional-scale numerical model simulations is used to conduct a diagnostic analysis of the cyclogenetic processes along the East Coast of the United States on 18 February 1979 that mark the initial development phase of the Presidents' Day cyclone. In this paper[4], data from a mesoscale model simulation are used to examine the processes which contribute to rapid cyclogenesis along the East Coast on 19 February 1979.

The specific purposes of this paper are: (1) to present a mesoscale model simulation of the Presidents' Day cyclone initialized at 1200 GMT 18 February that captures the upper-tropospheric intrusion of stratospheric air [marked by high potential vorticity (PV) values] upstream of the East Coast and the subsequent explosive development of the surface cyclone,

---

[4]This paper is based, to a large degree, on a paper recently submitted to Monthly Weather Review by Whitaker et al. (1987).

(2) to use the model simulation to examine the descent of the stratospheric air mass, as identified by Uccellini et al. (1985), and the interaction of this air mass with a lower-tropospheric PV maximum associated with an inverted trough and coastal front along the East Coast, and (3) to examine the processes that contribute to the rapid decrease of sea-level pressure and rapid increase in lower-tropospheric cyclonic vorticity during the explosive development phase of the cyclone.

A brief synoptic overview of the Presidents' Day cyclone is presented in Section 2. The model simulation is discussed in Section 3, with emphasis on the evolution of a polar jet (PJ)-trough system and its associated tropopause fold and a description of the simulated surface low. The high temporal and spatial resolution of the model is utilized to trace the movement of a PV maximum associated with the stratospheric air mass along sloping isentropic surfaces toward the East Coast in the 24 h preceding rapid cyclogenesis. The interaction of this PV maximum with a pre-existing low-level PV maximum along the East Coast is then examined. An evaluation of the various terms in the vorticity equation is presented in Section 4 to identify the processes contributing to the rapid increase in absolute vorticity during the explosive development phase of the storm. In Section 5, model-based trajectory computations are used to clarify the nature and origin of airstreams entering the low-level circulation associated with the rapid cyclogenesis. The results are then summarized in Section 6.

2.   SYNOPTIC OVERVIEW

As discussed in part I, the development of an inverted trough along the East Coast of the United States on 18 February 1979 marks the initial development phase of the Presidents' Day storm. By 00Z/19[5], a 1017 mb surface low formed along the coastal front-inverted trough off the Georgia coast (Fig. 1a). By 12Z/19, rapid cyclogenesis was in progress off the coast of Maryland (Fig. 1b), with heavy snowfall rates (5 to greater than 10 cm h^{-1}) occurring from Washington, DC, to New York City. The coastal cyclone then moved eastward over the Atlantic Ocean and developed into an intense vortex with hurricane-force winds, as the central sea-level pressure (SLP) decreased to 990 mb or lower by 00Z/20 (Fig. 1c). The rapid development phase of the storm is generally considered to have commenced between 06Z/19 and 12Z/19, and continued until at least 00Z/20.

---

[5]The time and date format used in this paper is consistent with that used in part I (i.e., 1200 GMT 19 February is abbreviated 12Z/19).
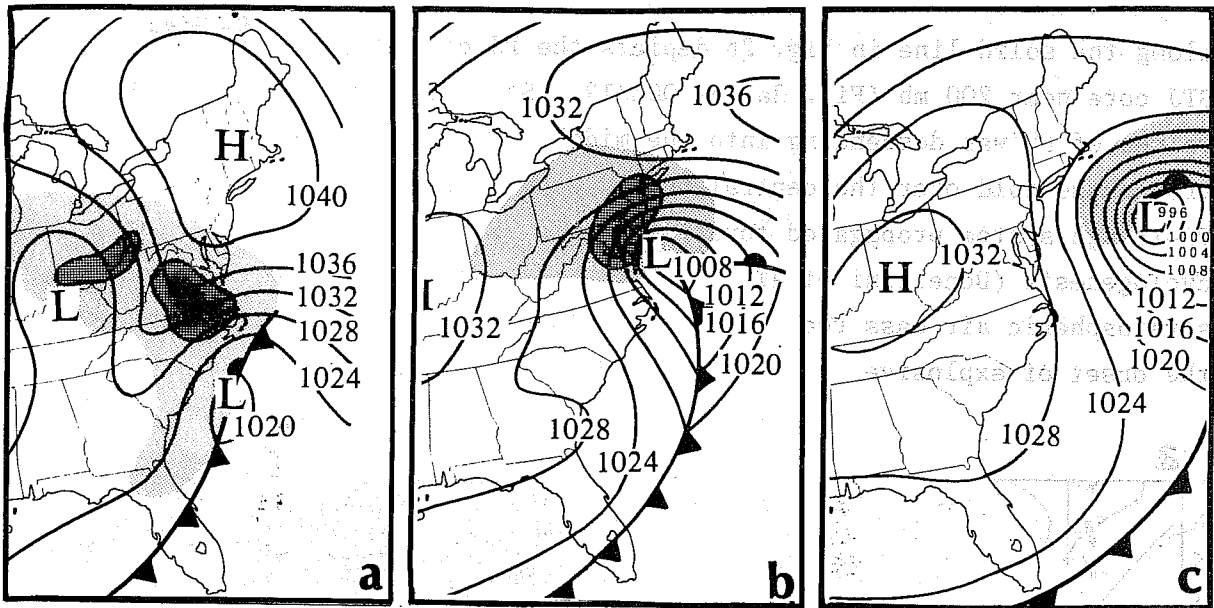
Fig. 1. *Sea-level pressure (mb) and surface frontal analyses for: (A) 0000 GMT 19 February, (B) 1200 GMT 19 February, and (C) 0000 GMT 20 February 1979. Shading indicates precipitation; dark shading indicates moderate to heavy precipitation.*
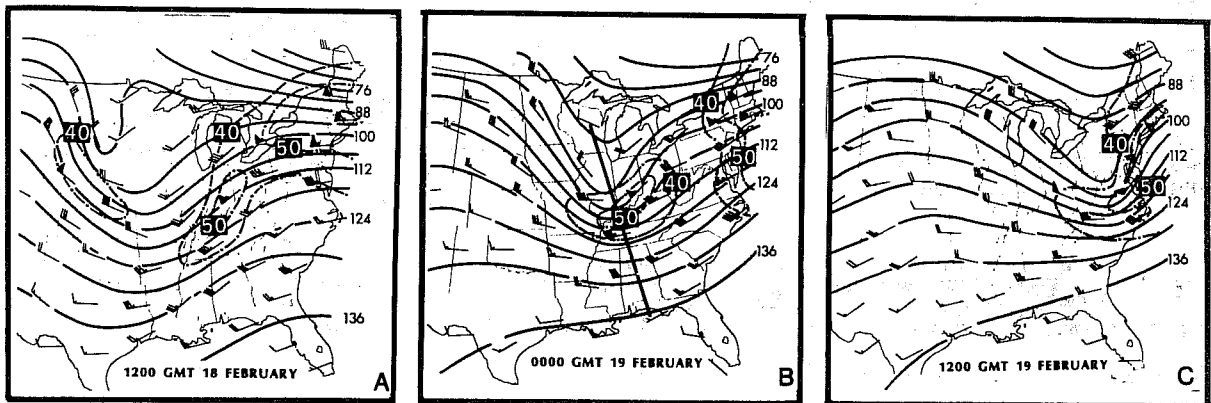

Fig. 2. *The 312 K analyses of Montgomery streamfunction (solid, 124 = 3.124 x 10^5 m^2 s^{-2}) and isotachs (dot-dashed, m s^{-1}) for: (A) 1200 GMT 18 February, (B) 0000 GMT 19 February, and (C) 1200 GMT 19 February 1979. Wind barbs represent observed wind speeds (whole barbs denote 10 m s^{-1}; half barbs 5 m s^{-1}). Solid line in (B) indicates position of cross section in Fig. 3.*

Aloft, the rapid development phase of the surface cyclone appears to be linked with the arrival of a PJ-trough system which propagated from the central United States at 12Z/18 (Fig. 2a) to the East Coast by 12Z/19 (Fig. 2c). Bosart and Lin's (1984) analysis of the semi-geostrophic PV and studies by Uccellini et al. (1984, 1985) indicate that the PJ-trough system was exerting a significant influence on the rapidly developing cyclone by 12Z/19. At 00Z/19, the trough and associated PJ, marked by wind speeds exceeding 50 m s^{-1} over the Ohio Valley (Fig. 2b), were poised just to the west of the cyclogenetic region (see Fig. 1a). A vertical cross section

along the solid line in Fig. 2b depicts the PJ centered near 300 mb and a STJ core near 200 mb (Fig. 3a) at 00Z/19. Stratospheric air marked by high values of PV was descending into the middle and lower troposphere within a tropopause fold over the central United States (Fig. 3b) as the amplifying PJ-trough system propagated toward the Ohio Valley, 12 h prior to rapid cyclogenesis (Uccellini et al., 1985). The PJ-trough system and descending stratospheric air mass reached the East Coast by 12Z/19, coinciding with the onset of explosive cyclogenesis (Uccellini et al., 1985).
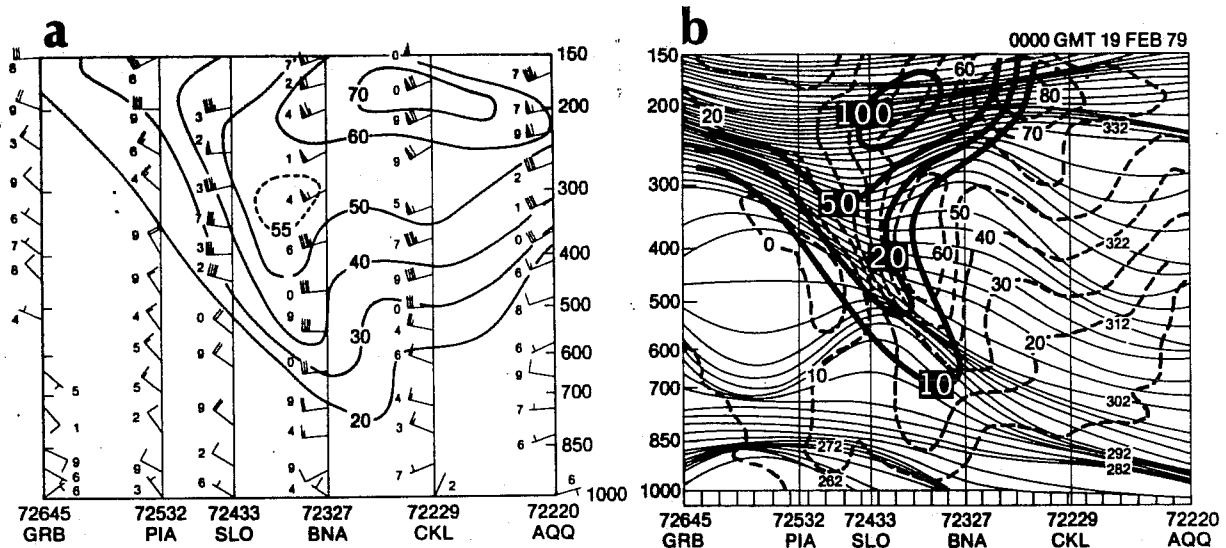

Fig. 3.   *Vertical cross section from Green Bay, Wisconsin (GRB), to Apalachicola, Florida (AQQ), for 0000 GMT 19 February 1979. (A) Isotach analysis for total wind speed (solid, m s^{-1}); wind barbs plotted as in Fig. 2 with last digit of observation. (B) Isentropes (solid, K), geostrophic wind speed normal to plane of cross section (dashed, m s^{-1}), and potential vorticity (dark solid where 10 = 10 x 10^{-6} K mb^{-1} s^{-1}).*

Bosart and Lin (1984) and Uccellini et al. (1985) provide detailed diagnostic analyses depicting the influence of the PJ-trough system on the surface cyclogenesis and associated precipitation prior to 12Z/19. However, the lack of data immediately off the coast prevents analyses during the explosive development phase of this storm following 12Z/19, which occurred primarily over the ocean. To account for the lack of data, results from a mesoscale model simulation are presented to provide insight into the physical processes that contributed to the explosive cyclogenesis over the western Atlantic Ocean for this case.

3.   MODEL SIMULATION

In this section, the structure of the simulated storm and the evolution of the simulated PJ-trough system and associated tropopause fold prior to and upwind of the cyclogenetic region are described. The MASS modeling system developed by Kaplan et al. (1982) and modified as described by Uccellini et al. (1987) is used for this simulation. The model simulation is initialized at 1200 GMT 18 February as described in part I.

3.1   Simulation of the storm

During the first 6 h of the model simulation (by 18Z/18), an inverted trough is forecast to develop off the Southeast Coast accompanied by coastal frontogenesis, which is represented by a strengthening of the temperature gradients along the coast (Fig. 4a). By 12 h (00Z/19), the coastal trough develops into a closed cyclonic circulation with a central pressure of 1020 mb (Fig. 4b), as compared with an observed central pressure of 1017 mb (Bosart, 1981). Heavy precipitation is concentrated along the Carolina coasts, with a small area of moderate to heavy precipitation also developing over northern Virginia between 03Z/19 and 06Z/19. The coastal low deepens to 1013 mb by 06Z/19 while moving northward to a position along the coastal border of North Carolina and Virginia (Fig. 4c). The central pressure drops 8 mb during the next 6 h, reaching 1005 mb at 12Z/19 [compared to 1006 mb in Bosart's (1981) analysis], while the storm moves to a position east of the Virginia-Maryland coast and the precipitation shield continues to spread north and east of the developing surface low (Fig. 4d). Heavy amounts of precipitation extend from southeastern Virginia to southern New Jersey.

Analyses of 700 mb relative humidity and vertical motion (Figs. 5a and 5b) at 12Z/19 illustrate the asymmetric structure of the storm. The southwestern sector of the storm is marked by dry subsiding air, while rising moist air is confined to the north and east of the storm system. A cross section bisecting the storm along a southwest-to-northeast plane (Fig. 5c) depicts a deep layer of subsidence on the cold side of the storm and a strong low-level ascent maximum just to the north and east of the low center. These asymmetries are also evident in the satellite imagery presented in Uccellini et al. (1985), which show that the deep cloud mass is confined to the north and east of the storm, while the minimum SLP is centered in a region free of deep clouds. Although other investigators have noted the similarity between the structure of the President's Day storm and that of tropical cyclones, the asymmetries in these analyses clearly indicate the fundamentally extratropical nature of the storm.
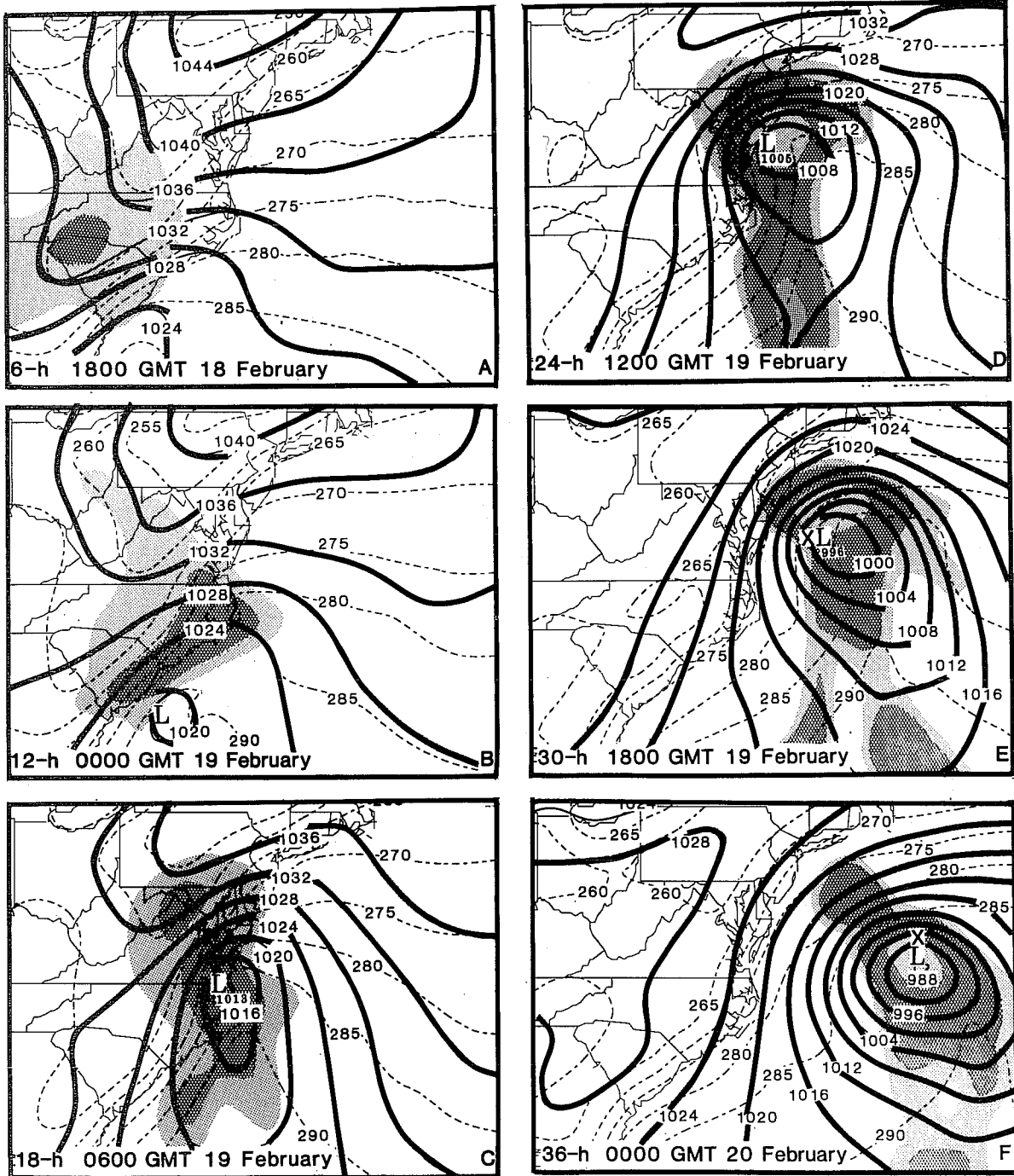
Fig. 4. *Sea-level pressure (solid, mb) and temperature on the lowest model level (dashed, K) from the model simulation at: (A) 6 h (1800 GMT 18 February), (B) 12 h (0000 GMT 19 February), (C) 18 h (0600 GMT 19 February), (D) 24 h (1200 GMT 19 February), (E) 30 h (1800 GMT 19 February), and (F) 36 h (0000 GMT 20 February). The lowest model level (σ = 0.9844) is about 29 mb above the surface. Fine shading indicates 6-h accumulated precipitation of 0.025 to 1 cm, coarse shading greater than 1 cm, during the 6 h ending at the time indicated on each panel.*
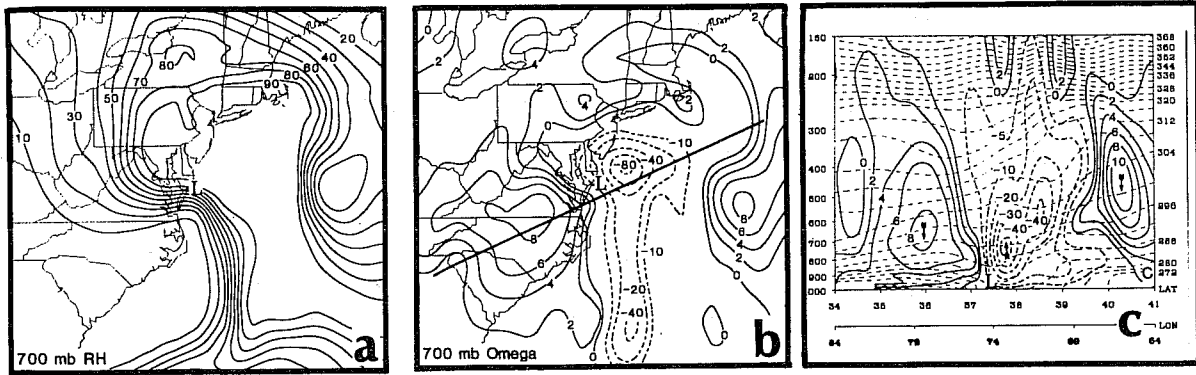
Fig. 5. *The 700 mb analyses of: (A) relative humidity (percent) and (B) omega ($\mu b \ s^{-1}$) at 24 h (1200 GMT 19 February). (C) is a cross section of potential temperature (dashed, K) and omega [solid-positive, dashed-negative ($\mu b \ s^{-1}$)] along solid line in (B). Note: Contour intervals for negative contours in (C) are irregular for legibility.*

After 12Z/19, the simulated storm center takes a more easterly track, deepening 9 mb between 12Z/19 and 18Z/19 to 996 mb (Fig. 4e) and 8 mb between 18Z/19 and 00Z/20 to 988 mb (Fig. 4f). While it is difficult to pinpoint the exact central pressure and location of the actual surface low over the ocean, a comparison with Bosart's (1981) analyses (see his Fig. 3) indicates that the deepening rate of the simulated cyclone may be less than the actual storm system after 12Z/19, since the simulated cyclone has a central pressure of 996 mb at 18Z/19, which compares to Bosart's analyzed central pressure of 990 mb at the same time. Meanwhile, the track of the simulated cyclone deviates from the track of the actual storm by perhaps only 110 km between 12Z/19 and 00Z/20 (see Figs. 4e and 4f). The model SLP fields in Fig. 4 indicate a continuous deepening of the simulated storm system during the entire 36-h forecast period, with an enhancement of the deepening rate after 00Z/19.

Analyses of the SLP tendencies and mass divergence profiles are shown to illustrate a transition throughout the depth of the troposphere which accompanies the rapid development of the simulated storm system. The mass divergence in σ coordinates is related to the surface pressure tendency through the equation

$$\frac{\partial p_s}{\partial t} = + \int_{\sigma=1}^{\sigma=0} \nabla_\sigma \cdot (\frac{\partial p}{\partial \sigma} \underline{V}) d\sigma \ , \tag{1}$$

where ∂p is a measure of the mass between σ surfaces and $\underline{V}$ is the two-dimensional horizontal wind velocity. The 3-h pressure tendencies and vertical profiles of the mass flux divergence are depicted in Fig. 6 for 3-h time increments between 06Z/18 and 15Z/19. The mass divergence is averaged over 30 grid points represented by the shaded area in each map inset.
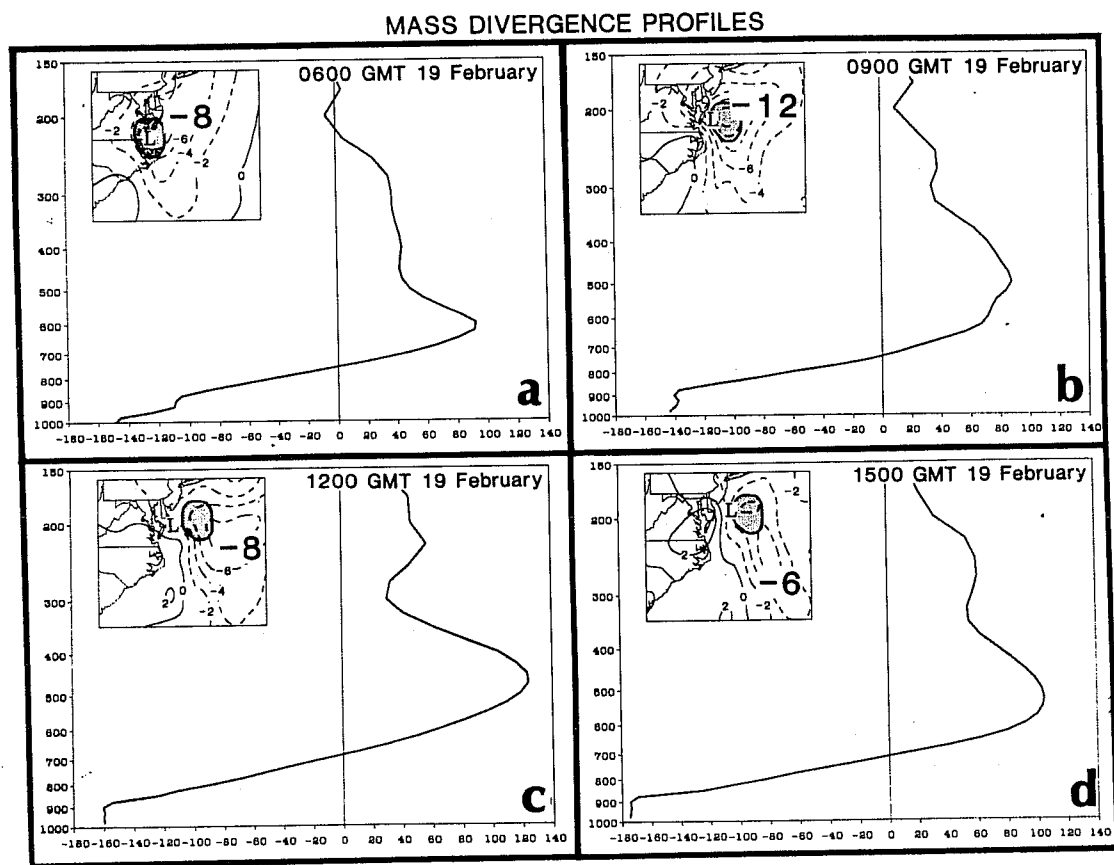
MASS DIVERGENCE PROFILES

Fig. 6. *Area-averaged vertical profiles of mass divergence (10 = 10 x 10⁻³ mb s⁻¹) computed for: (A) 18 h into the forecast (0600 GMT 19 February), (B) 21 h (0900 GMT 19 February), (C) 24 h (1200 GMT 19 February), and (D) 27 h (1500 GMT 19 February) during the explosive deepening phase. The profiles are computed for shaded regions depicted on map inset for each time. The 3-h pressure changes (mb) and locations of the surface low center are depicted on each map inset.*

By 03Z/19 (not shown), mass convergence extends over a deep layer in the low levels in conjunction with the developing cyclone and a broadly defined maximum in the mass divergence becomes established above 800 mb, with the maximum mass divergence located near the 600 mb level. The maxima of the upper-level mass divergence and lower-level mass convergence appear to both increase in magnitude between 06Z/19 and 15Z/19 (Figs. 6a-6d). This two-layer structure is similar to the schematic profiles deduced for extratropical systems by Bjerknes and Holmboe (1944) and shown in more

130

recent budget studies [for example, Johnson and Downey (1975)]. The
continued deepening of the simulated surface low after 03Z/19 (note the SLP
tendencies in the map insets in Fig. 6) appears to be associated with an
increase in magnitude of the mass divergence between the 700 and 500 mb
levels. The profiles in Fig. 6 demonstrate that the rapid deepening of the
surface cyclone is associated with a changing mass divergence profile
through a large depth of the troposphere. Furthermore, the amplification
in the mass divergence (convergence) in the upper (lower) troposphere
coincides with (1) a significant increase in the precipitation rates and
(2) the arrival of the PJ-trough system from the west, as described below.

3.2   Simulation of the PJ-trough system and associated tropopause fold
   upstream and prior to rapid cyclogenesis

Since Kleinschmidt's initial assertion that the stratospheric reservoir of
PV "is essentially the producing mass of cyclones" (Eliassen and
Kleinschmidt, 1957, p. 125), a growing number of papers have provided
evidence for the influence of stratospheric extrusions in surface
cyclogenesis [e.g., see Danielsen (1968), Bleck (1973), Bleck and Mattocks
(1984), Uccellini et al. (1985), and Hoskins et al. (1985)]. Uccellini et
al. (1985) describe that the evolution of the Presidents' Day storm is
marked by the downward extrusion of stratospheric, high PV air along the
axis of the intensifying polar jet streak over the Northern Plains on 18
February 1979 (prior to cyclogenesis along the East Coast), which
subsequently descends and translates eastward toward the developing surface
cyclone by 12Z/19. Isentropic maps and vertical cross sections derived
from the model data are now presented to provide further insight into the
temporal evolution and structure of the PJ-trough system and associated
tropopause fold and its subsequent influence on the cyclogenesis along the
East Coast[6].

At the time of initialization (12Z/18), the PJ on the 312 K surface is
located near the inflection point on the west side of the trough over the
middle of the United States, with maximum wind speeds exceeding 45 m s^{-1}
over Nebraska (Fig. 2a) and large values of PV [defined by the expression
$(\zeta_\theta + f)\partial\theta/\partial p$] evident on the cyclonic side of the jet [see Fig. 9b in

---

[6]All diagnostic and predicted quantities presented in this paper were
interpolated horizontally from the model domain to a 0.5° latitude-
longitude grid by overlapping quadratic polynomials and vertically by
linear variation in σ to isentropic surfaces at 4 K increments and to
pressure surfaces at 50 mb increments.

Uccellini et al. (1985)]. The vertical cross sections across the axis of the PJ at 12Z/18 (Uccellini et al., 1985) show that stratospheric values of PV [defined to be greater than 10×10^{-6} K mb^{-1} s^{-1} by Reed and Danielsen (1959)] extend downward within a region of strong subsidence centered on the warm side of an upper-tropospheric frontal zone. Numerous studies (Reed, 1955; Reed and Danielsen, 1959; Danielsen, 1968; Shapiro, 1970, 1975; Uccellini et al., 1985; Keyser and Shapiro, 1986) have established that upper-level frontogenesis and tropopause folding are consequences of subsidence that is maximized beneath the axis of a jet streak and within and to the warm side of the developing frontal zone.

At 18Z/18, the simulated PJ and its associated PV maximum propagate southeastward toward the base of the trough located in eastern Missouri on the 312 K surface (Figs. 7a and 7b). Maximum wind speeds in the jet core increase to slightly over 50 m s^{-1}. Temperature gradients in the upper-tropospheric frontal zone strengthen, and strong subsidence (not shown) within and to the warm side of the baroclinic zone continues to transport stratospheric air marked by high values of PV down below the 600 mb level (Fig. 7c).

By 03Z/19, the PJ is located over Kentucky and the PV maximum is centered over the Ohio-Indiana border (Figs. 8a and 8b). The cross section (Fig. 8c) illustrates that the PJ is still undercutting the position of the STJ, with the PJ now evident as a downward extension of the 50 m s^{-1} isotach. Temperature gradients continue to increase within the frontal zone, where PV values are large. The extrusion of stratospheric values of PV nearly reaches the 700 mb level (Fig. 8c), as subsidence continues all along the frontal zone (not shown).

These isentropic maps and cross sections show: (1) the intensification of maximum wind speeds within the simulated PJ between 12Z/18 and 00Z/19, (2) the intensifying middle- and upper-tropospheric frontal zone supporting the PJ upstream of and prior to the rapid cyclogenesis, and (3) the descent of stratospheric values of PV to near 700 mb by 03Z/19 within the frontal zone occurs upstream of the rapid cyclogenetic region along the East Coast.
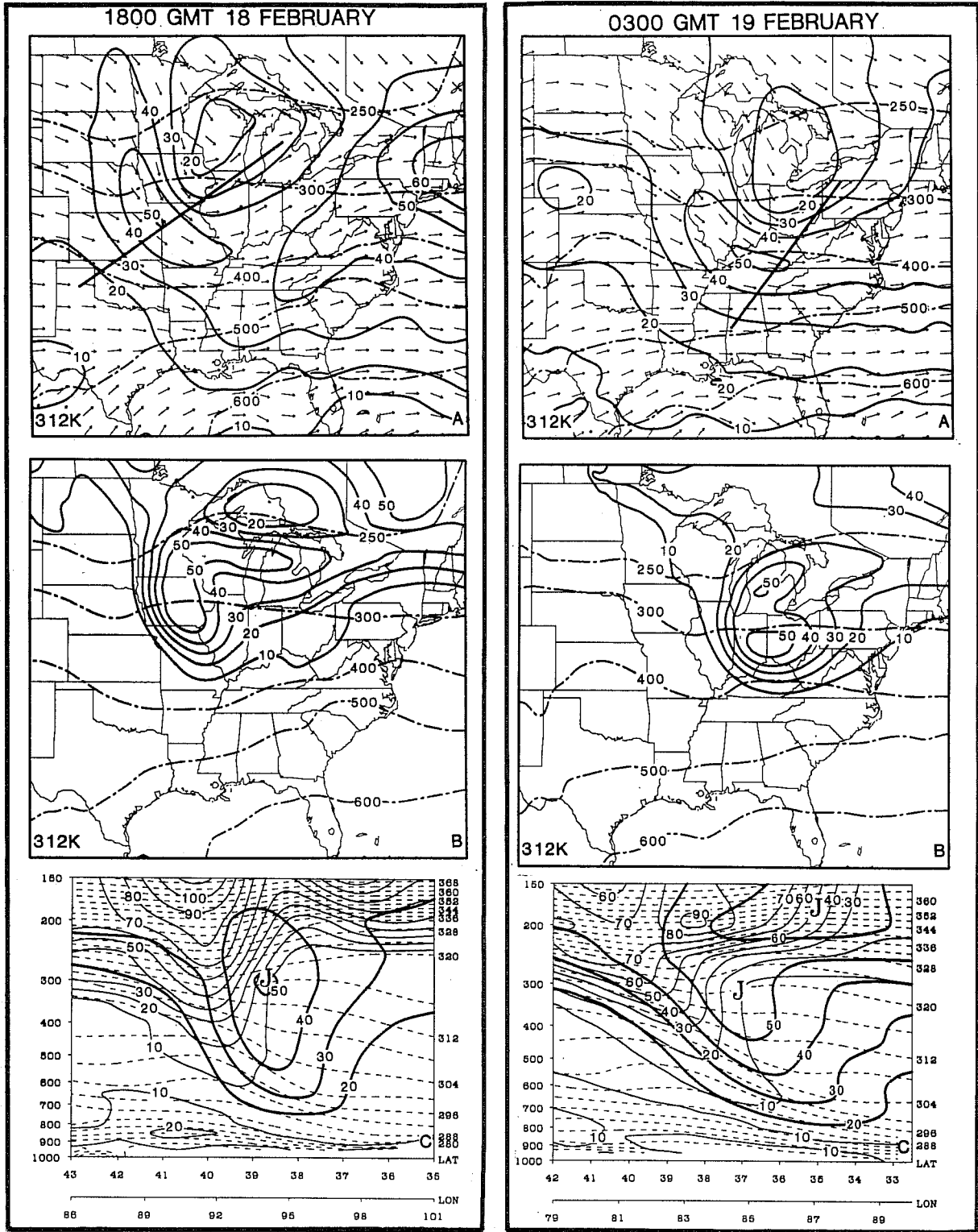
Fig. 7. [Left] *Isentropic analyses for 312 K surface and vertical cross section at 6 h (1800 GMT 18 February): (A) isotachs (solid, m s^{-1}), pressure (dot-dashed, mb), and arrows to indicate wind direction; (B) pressure (dot-dashed, mb) and potential vorticity (solid, 10 = 10 x 10^{-6} K mb^{-1} s^{-1}); and (C) isentropes (dashed, K), potential vorticity (thin solid, 10 = 10 x 10^{-6} K mb^{-1} s^{-1}), and isotachs (heavy solid, m s^{-1}). "J" in (C) indicates position of jet core. Line in (A) indicates position of cross section.*

Fig. 8. [Right] *As in Fig. 7 at 15 h (0300 GMT 19 February).*

133

3.3   Interaction of the stratospheric extrusion with a low-level PV

maximum

The eastward propagation and downward extrusion of the stratospheric air
mass to a position several hundred kilometers northwest of the developing
cyclonic circulation at 03Z/19 can be resolved easily due to the increased
spatial and temporal resolution provided by model data, allowing a distinct
path to be traced. This path was previously inferred using the operational
radiosonde analyses and the once-per-day ozone measurements from the Total
Ozone Mapping Spectrometer (TOMS) (Uccellini et al., 1985). Uccellini et
al. (1985) and Bosart and Lin (1984) also show a lower-tropospheric "in-
situ" PV maximum associated with the coastal front/inverted trough on 18
February prior to the explosive cyclogenesis on 19 February. Trajectory
results from Uccellini et al. (1985) indicate that air from this secondary
maximum was ascending and interacting with the descending stratospheric air
mass over Virginia by 12Z/19.

The 300 K isentropic PV maps (Fig. 9) from the model simulations for the
period between 06Z/19 and 15Z/19 depict the interaction of the PV maximum
associated with the descending stratospheric air mass with a PV maximum
confined to the lower-tropospheric circulation along the coast. The
sloping 300 K surface follows the descent of the stratospheric PV maximum
toward the lower troposphere off the East Coast. Cross sections through
the PV maxima (Fig. 10) illustrate the vertical structure of the
stratospheric air mass and its interaction with the lower-tropospheric PV
maximum.

At 06Z/19, the stratospheric PV maximum is located over West Virginia at
the 450 to 500 mb level (Fig. 9a). The cross section oriented through the
two PV maxima (indicated by the solid line in Fig. 9a) shows the descending
stratospheric air mass as a distinct separate entity from a low-level PV
maximum along the coast (Fig. 10a). By 09Z/19, the lower-tropospheric PV
maximum becomes more evident along the Virginia coast (as the 300 K surface
descends to higher pressure), with the stratospheric PV maximum approaching
it from the west (Fig. 9b). The upper-level maximum begins to decrease
slightly in magnitude as it crosses Virginia, a characteristic that is
likely due to diabatic effects associated with the expanding precipitation
shield in this region. However, it continues to move eastward down the
sloping 300 K surface where the 10×10^{-6} K mb^{-1} s^{-1} isopleth merges with
the low-level coastal PV maximum. The merging of these two PV maxima just
off the East Coast coincides with the onset of rapid deepening of the
simulated cyclone. By 12Z/19 (Fig. 9c), the two PV maxima on the 300 K
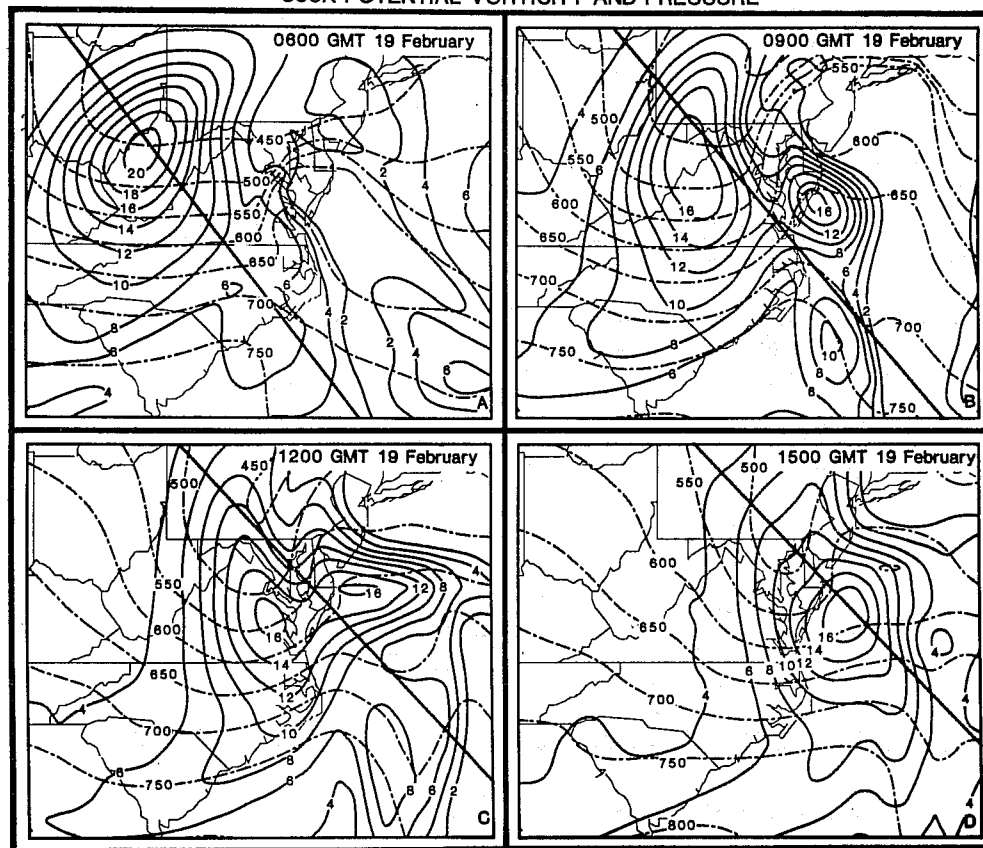
300K POTENTIAL VORTICITY AND PRESSURE

Fig. 9. *The 300 K analyses of potential vorticity (solid, 10 = 10 x 10^{-6} K mb^{-1} s^{-1}) and pressure (dot-dashed, mb) at: (A) 18 h (0600 GMT 19 February), (B) 21 h (0900 GMT 19 February), (C) 24 h (1200 GMT 19 February), and (D) 27 h (1500 GMT 19 February). Lines indicate position of cross sections in Fig. 10.*

surface are enclosed by a 14 x 10^{-6} K mb^{-1} s^{-1} isopleth. By 15Z/19 (Fig. 9d), a single PV maximum is evident off the Maryland coast.

The cross sections in Fig. 10 (denoted by the solid lines in Fig. 9) illustrate the merging of the upper- and lower-tropospheric PV maxima above the developing cyclone. At 09Z/19 (Fig. 10b), the 10 x 10^{-6} K mb^{-1} s^{-1} isopleth of PV extends downward along the upper-tropospheric frontal zone toward the 700 mb level just to the northwest of the lower-level PV maxima. By 12Z/19, the 10 x 10^{-6} K mb^{-1} s^{-1} isopleths have connected and, by 15Z/19, the upper-level PV maximum almost overlies the surface cyclone and the associated tongue of high PV extends directly into the low-level maximum of PV (Fig. 10d).
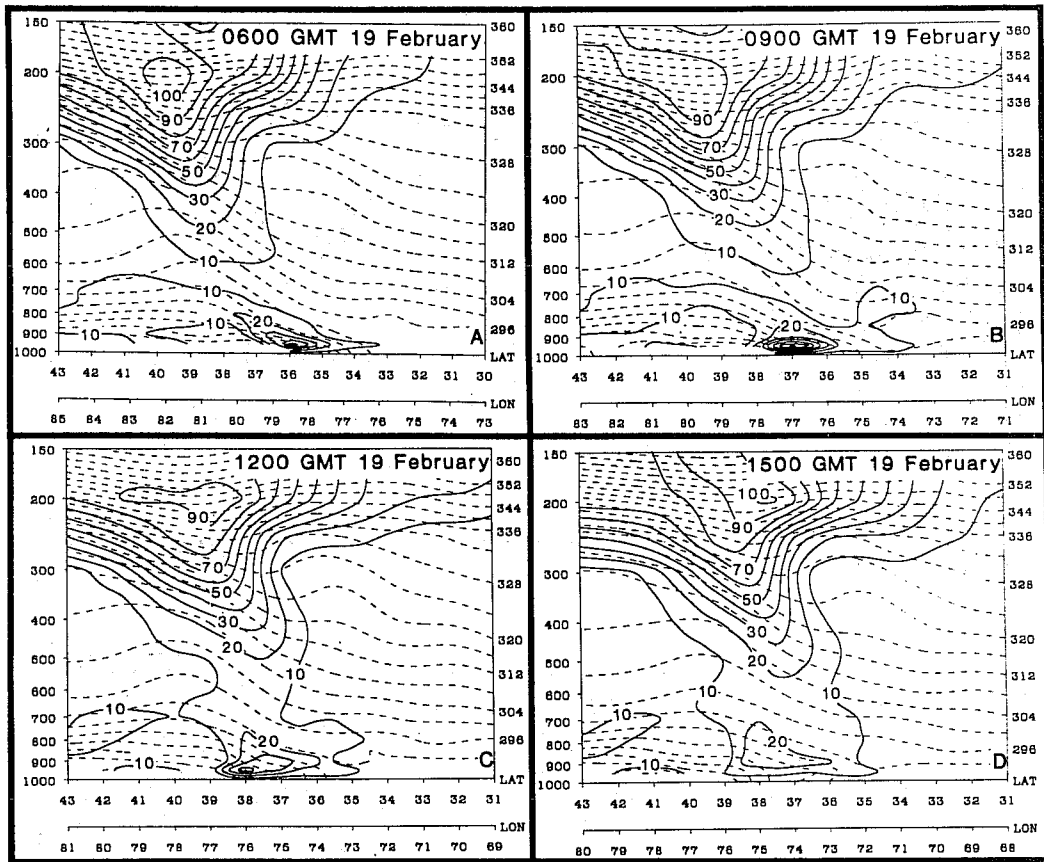
Fig. 10. *Vertical cross sections of potential temperature (dashed, K) and potential vorticity (solid, 10 = 10 x 10^{-6} K mb^{-1} s^{-1}) at: (A) 18 h (0600 GMT 19 February), (B) 21 h (0900 GMT 19 February), (C) 24 h (1200 GMT 19 February), and (D) 27 h (1500 GMT 19 February). Lines in Fig. 9 indicate positions of cross sections.*

3.4 Summary of the model simulation description

On the basis of the Eulerian analyses presented in this section, it appears that the onset of rapid deepening of the surface cyclone in this simulation commences after 03Z/19 and proceeds through the rest of the model simulation to 00Z/20 (see Table 1). The explosive development in the model simulation is marked by (1) SLP decreases of approximately 2 mb h^{-1} at the center of the storm; (2) a transition in the vertical profile of the area-averaged mass divergence to a two-layer structure, with the maximum mass divergence amplifying within the 500 to 700 mb layer; (3) an increase in the precipitation rates, especially those associated with the grid-resolvable precipitation between 06Z and 09Z just to the north and west of the storm center (see Table 1); and (4) the arrival of a PV maximum of stratospheric origin, which merges with a PV maximum that is located in the lower troposphere and is associated with the coastal front and inverted

136

Table 1. Listing of sea-level pressure (SLP) minimum and pressure tendency at center of simulated cyclone, the 3-h precipitation maxima (cm) from the grid-resolvable precipitation north and west of the storm center, and the 850 mb absolute vorticity maximum.

Time	Min SLP (mb)	6-h SLP Tendency	3-h Precipitation Max Grid-Resolvable (cm)	850 mb Max Vorticity 10^{-5} s^{-1}
12Z/18	1029			12
15Z/18	1026	-6	0.84	20
18Z/18	1023		0.64	26
21Z/18	1021	-3	1.22	27
00Z/19	1020		0.91	27
03Z/19	1018	-7	0.84	35
06Z/19	1013		1.55	37
09Z/19	1007	-8	4.06	56
12Z/19	1005		5.84	62
15Z/19	1002	-9	5.33	60
18Z/19	996		4.83	59
21Z/19	992	-8	2.46	57
00Z/20	988		0.79	62

trough. The interaction between PV maxima of stratospheric and lower-tropospheric origins is consistent with the concept of "type B" cyclogenesis, defined by Petterssen and Smebye (1971) to categorize rapid cyclogenesis when an upper-level trough overtakes a low-level baroclinic zone.

Table 1 also shows that the rapid deepening of the simulated storm system is marked by an increase in the 850 mb absolute vorticity from 37 x 10^{-5} s^{-1} at 06Z/19 to 56 and 62 x 10^{-5} s^{-1} at 09Z/19 and 12Z/19, respectively. Eulerian and Lagrangian diagnostics are presented in the following sections to (1) investigate the processes that contribute to the rapid increase of lower-tropospheric absolute vorticity after 06Z/19 and (2) illustrate the nature and origin of different airstreams which converge into the rapidly developing low-level circulation during the rapid development phase.

4. VORTICITY DIAGNOSTICS FROM A EULERIAN PERSPECTIVE

The vertical component of the inviscid vorticity equation in pressure coordinates is

$$\frac{\partial(\zeta + f)}{\partial t} = -\vec{V} \cdot \nabla(\zeta + f) - \omega\frac{\partial \zeta}{\partial p} - (\zeta + f)\nabla \cdot \vec{V} - \hat{k} \cdot (\nabla\omega \times \frac{\partial \vec{V}}{\partial p}) , \qquad (2)$$

where ζ is the vertical component of the relative vorticity, $\vec{V}$ is the horizontal wind vector, and ω is the vertical wind speed. The local rate of change of ζ is given by the sum of the horizontal advection of absolute vorticity, the vertical advection of relative vorticity, the generation by horizontal convergence (or stretching), and the tilting of horizontal components of vorticity into the vertical by gradients of vertical motion. These four terms will hereafter be referred to as the horizontal advection, vertical advection, stretching, and tilting terms.

Analyses of the absolute vorticity, the vorticity tendency, and the relative magnitudes of each term of eq. (2) during the period of explosive deepening reveal that the stretching term dominates the other terms in contributing to the rapid increase of vorticity in the lower troposphere (Whitaker et al., 1987). A vertical cross section through the region of maximum vorticity increase [Fig. 11; see Fig. 14c2 in Whitaker et al. (1987)] illustrates the vertical distribution of these terms. The vorticity tendency is maximized below 700 mb (Fig. 11b), due to the dominance of stretching at lower levels (Fig. 11e). Above 700 mb, the stretching term becomes negative, which is consistent with the increasing mass divergence in the middle to upper troposphere (Fig. 6c). The horizontal vorticity advection is positive in the middle troposphere ahead of the advancing short-wave trough, indicating that quasi-geostrophic forcing as diagnosed by Bosart and Lin (1984) utilizing radiosonde data also exists above the simulated surface low at this time. The tilting term is also positive to the south and east of the developing storm in this cross section. Finally, the vertical advection term is large in the 700 to 500 mb layer, suggesting that the strong ascent maximum north of the surface low (Fig. 5b) in a region of significant precipitation is advecting the lower-tropospheric vorticity upward into the middle troposphere (although this positive effect is offset by negative stretching and tilting in the middle troposphere). This result is consistent with the Johnson and Downey (1976) angular momentum budget study which shows that, for an extratropical cyclone, the mid-level vortex develops and is maintained, in part, due to to the vertical transport of absolute angular momentum by a meridional mass circulation enhanced by the release of latent heat.
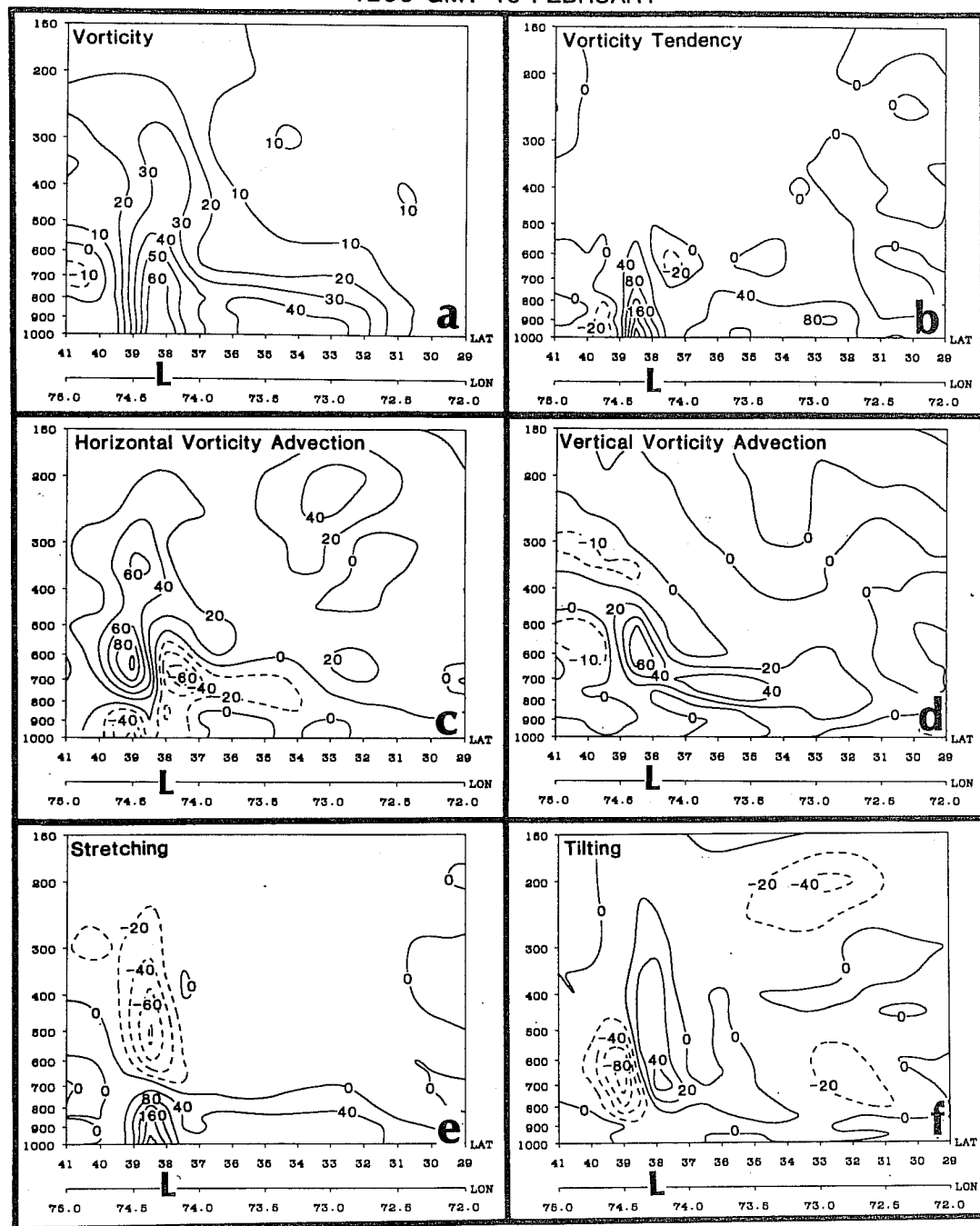
Fig. 11. Cross sections at 24 h (1200 GMT 19 February) of: (A) absolute vorticity, (B) vorticity tendency, (C) horizontal advection of vorticity, (D) vertical advection of vorticity, (E) stretching, and (F) tilting. In (A), 10 = 10 x 10^{-5} s^{-1}; in (B), (C), (D), (E), and (F), 10 = 10 x 10^{-9} s^{-2}. The position of the cross section extends nearly in a north-south line through the surface low-pressure center at 38° N.

139

5.   DIAGNOSTICS FROM A LAGRANGIAN PERSPECTIVE AND THE ANALYSIS OF VARIOUS AIRSTREAMS DURING RAPID CYCLOGENESIS

From the analyses in Section 3 and the summary in Table 1, it appears that the explosive deepening (decrease in SLP) and rapid spinup in the lower troposphere (increase in the 850 mb vorticity) occur as two distinctly different PV maxima merge. Trajectories are now presented to depict this interaction before and during the rapid development phase of the Presidents' Day storm.

5.1   Trajectories computed backward in time from the region of surface cyclogenesis

A history file containing data at 15 min intervals during the model integration is used to compute back trajectories over a 36-h period for a number of parcels initialized on a 2° by 2° box surrounding the developing surface low and the 850 mb vorticity tendency maximum at 03Z/19, 06Z/19, 09Z/19, and 12Z/19 (Fig. 12), which includes the period during which rapid cyclogenesis commences. Forty parcels were initialized along the perimeter of each box at each time, ten on a side at evenly spaced intervals. Trajectories were computed using the predicted u, v, and omega output[7].

The back trajectories from the box located at 700 mb initialized at 03Z/19 and 06Z/19 (Figs. 12a and 12b) show that during this period the air within the entire storm volume at 700 mb generally originates within the oceanic PBL between 880 and 985 mb. These parcels ascend and accelerate toward the developing storm system beneath the region of, and probably in response to, the mass flux divergence that is contributing to the decreasing SLP within the box (i.e., Fig. 6a). Between 06Z/19 and 09Z/19 (Fig. 12c), a major transition has occurred with the arrival of an airstream from the west-southwest into the region of what is now a rapidly developing cyclone. This airstream originates from near the 500 mb level within the PJ/ tropopause fold region in the central United States and approaches the

---

[7]New parcel positions were computed using an iterative method. A first-guess position was computed using a simple forward time step with the velocity components at the original position. New velocity components (obtained by interpolating to the first-guess position at the new time) were averaged with the old velocity components, and an updated position was obtained with these averaged velocities. This process was repeated three times for each time step.

storm from the southwest while the ocean-influenced airstreams dominate the southeastern, eastern, and northern sides of the storm system. By 12Z/19 (Fig. 12d), the airstream originating near the 400 mb level within the PV maximum (associated with the tropopause fold) and descending toward the storm center becomes an increasingly important component of the storm system during the simulated period of rapid cyclogenesis.

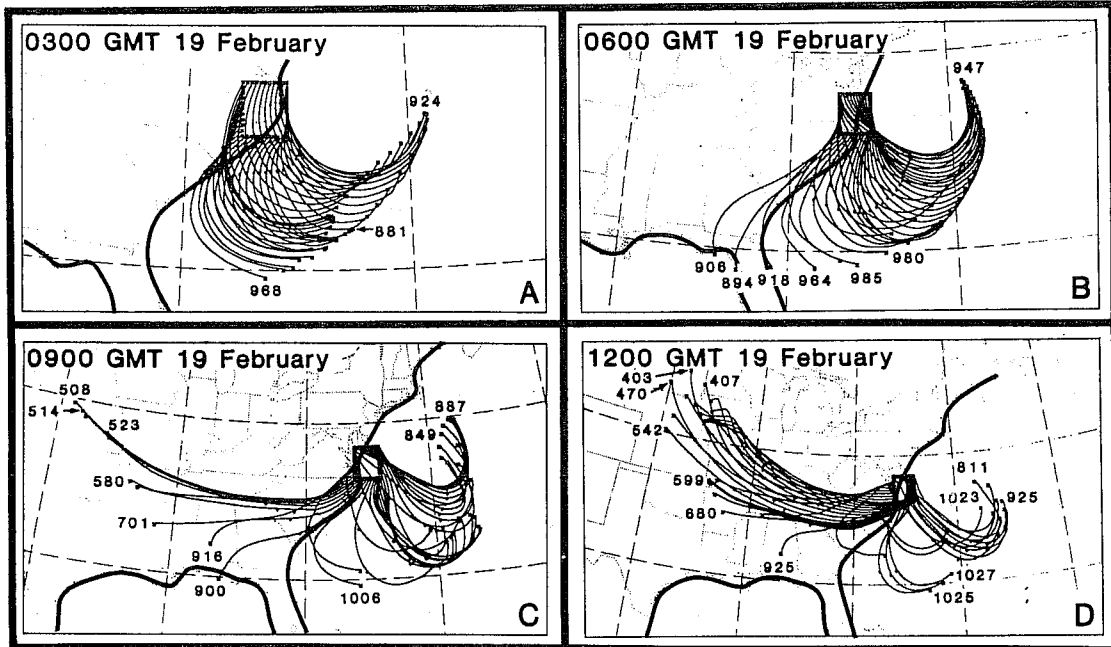## BACK TRAJECTORIES INITIALIZED ON THE 700 MB LEVEL

Fig. 12. *Paths of 40 model trajectories initialized on a 2° by 2° box surrounding the maximum of vorticity tendency on the 700 mb level at (A) 0300 GMT 19 February, (B) 0600 GMT 19 February, (C) 0900 GMT 19 February, and (D) 1200 GMT 19 February computed backward in time to 1200 GMT 18 February. The pressure in mb is given at the beginning point of selected trajectories.*

The model-based trajectories confirm that the rapid development phase of the Presidents' Day cyclone ensued as two distinctly different airstreams converged toward the storm center between 03Z/19 and 12Z/19. Carlson (1980) describes these airstreams as the "dry airstream" descending from the west and the "cold conveyor belt" ascending from the east. At 12Z/19 (Fig. 12d), there is also an indication of a "warm conveyor belt," also described by Carlson, consisting of air originating south of the storm and rising as it approaches the storm system. Although the airstream appears to be comparatively weak (made up of only 3 out of the 40 parcels in Fig. 12d), its ascent to a position near 700 mb on the northern boundary of the box at 12Z/19 with stratospheric air descending to the 700 mb level on the western, southwestern, and southern portions of the box (Fig. 12d) is in agreement with the trajectories computed from the radiosonde data base and described by Uccellini et al. (1985).

141

The origin and history of these airstreams has an important effect on the distribution of moisture and precipitation. The descent of parcels from the central United States toward the southwest quadrant of the storm agrees with the analyzed dry intrusion at 700 mb (Fig. 5a). On the other hand, the long track of the parcels within or just above the ocean-influenced PBL (where sensible heat and moisture fluxes are large) and the ascent of parcels within the cold conveyor belt north and east of the storm center are both consistent with the region of high relative humidity (Fig. 5a) and heavy precipitation (Fig. 4d). The asymmetric distribution of moisture and vertical velocity fields illustrated in Fig. 5, as well as the asymmetric cloud distribution observed in satellite imagery [see Figs. 2, 3, and 4 in Uccellini et al. (1985)], are related to the motion of these widely differing airstreams.

Representative trajectories selected from the dry airstream, cold conveyor belt, and warm conveyor belt are shown in Figs. 13a and 13b. In the remainder of the section, these trajectories, along with diagnostic quantities presented in tabular form, are described to provide insight as to how these different airstreams interact and contribute to the development of the simulated storm system. A more thorough description is provided by Whitaker et al. (1987).

5.2 Trajectory diagnostics for the dry airstream

A subset of the trajectories representative of the dry airstream is illustrated in Fig. 13a. These trajectories (1-3) spread out as they descend and move east-southeastward, consistent with the schematic for typical trajectories which accompany tropopause folding presented by Danielsen (1980, Fig. 12) and with the trajectories computed for this case using the operational radiosonde data base (Uccellini et al., 1985).

Trajectory 2 was chosen to represent parcels which trace back from the southwestern quadrant of the developing storm at 15Z/19 to the tropopause fold over the Northern Plains 27 h earlier. Diagnostic variables interpolated to the parcel positions are listed in Table 2. This trajectory originates at 470 mb over western Iowa, below the axis of the intensifying PJ and within the stratospheric extrusion associated with the tropopause fold as indicated by a high value of PV (13.1×10^{-6} K mb^{-1} s^{-1}) and low specific humidity [0.2 g kg^{-1} (not shown)]. For the most part, the PV and potential temperature are conserved as the parcel descends to the
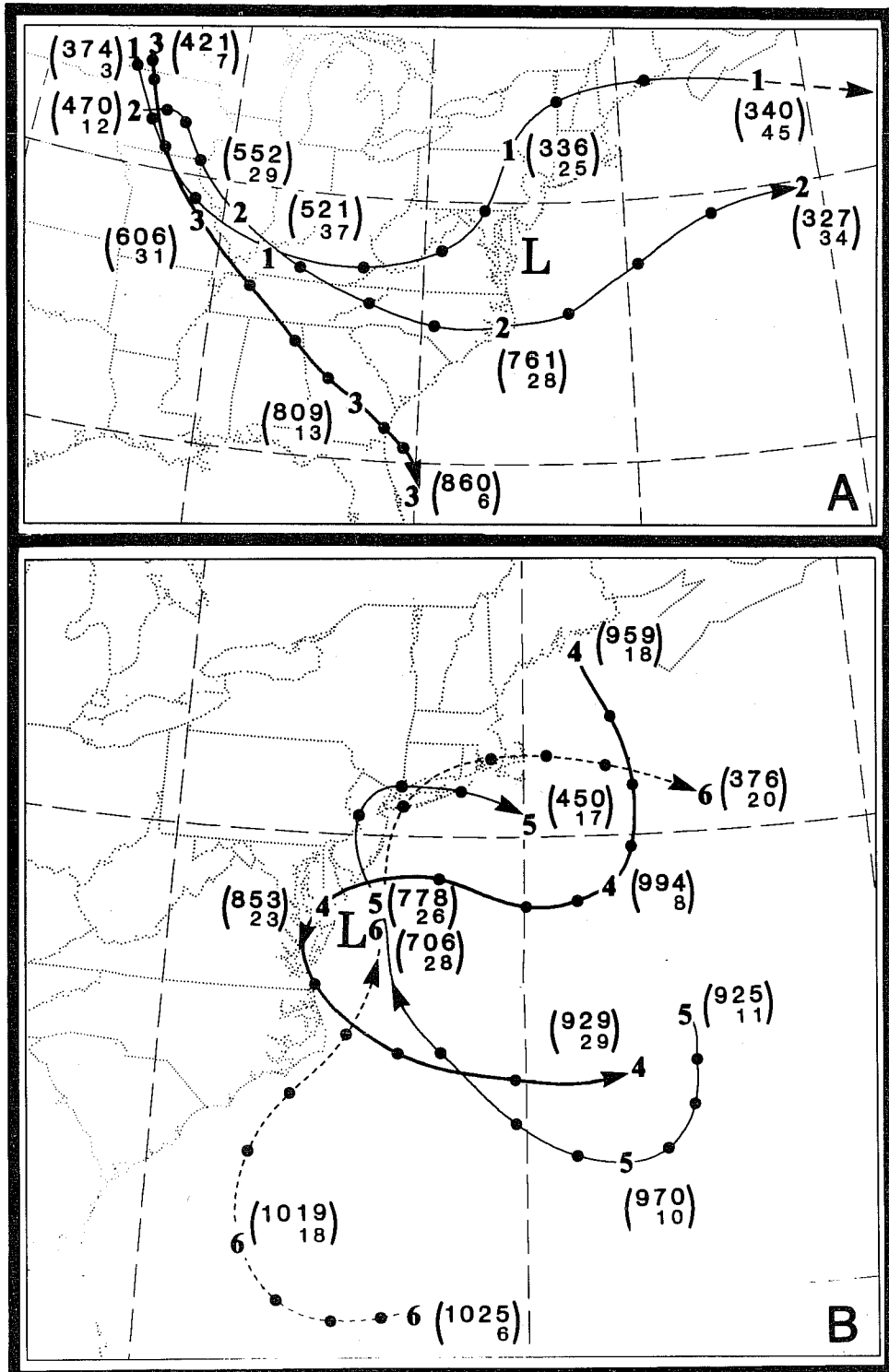
36-HOUR TRAJECTORIES

Fig. 13. *A collection of six 36-h trajectories computed forward from 1200 GMT 18 February. Trajectory numbers (1-6, bold) are placed at 12-h intervals along the trajectory. Large dots mark 3-h positions. Pressure (mb) and speed (m s^{-1}) are given inside parentheses at 12-h intervals. "L" denotes position of surface low at 1200 GMT 19 February.*

761 mb level by 12Z/19.[8] Between 12Z/19 and 15Z/19, the PV, θ, $\zeta + f$, and stretching all increase as the parcel passes through the top of the lower-tropospheric PV maximum along the East Coast (Fig. 10c). The PV increases to a value of 15.1×10^{-6} K mb^{-1} s^{-1} by 15Z/19, while the static stability decreases from 0.065 K mb^{-1} at 12Z/19 to 0.053 K mb^{-1} at 15Z/19, indicating that the parcel is entering the boundary layer PV maximum. At the same time, the stretching term increases from 0.7×10^{-9} s^{-2} to as high as 13.2×10^{-9} s^{-2} at 14Z/19, as the parcel begins to accelerate up and out of the storm system. The tilting term remains negative, except for a brief period, and does not contribute appreciably to the spinup associated with this airstream. At 15Z/19, the parcel attains a maximum absolute vorticity of 3.2×10^{-4} s^{-1} at a pressure of 714 mb. The vorticity then decreases as the parcel rises through a layer of strong divergence above 700 mb, as indicated by the negative stretching after 15Z/19 in Table 2.

Table 2. Listing for the dry airstream trajectory (trajectory 2 in Fig. 13a) for the times listed in the left-hand column. The variables include: pressure (p, mb), potential temperature (θ, K), static stability ($-\partial\theta/\partial p$, K mb^{-1}), potential vorticity (PV, $10 = 10 \times 10^{-6}$ K mb^{-1} s^{-1}), isobaric absolute vorticity ($\zeta_p + f$, 10^{-5} s^{-1}), and the stretching and tilting terms interpolated to parcel positions ($10 = 10 \times 10^{-9}$ s^{-2}).

DRY AIRSTREAM (TRAJECTORY 2)

Time	p mb	θ K	Stability $-$K mb^{-1}	PV 10^{-6} K mb^{-1} s^{-1}	$\zeta_p + f$ 10^{-5} s^{-1}	Stretch 10^{-9} s^{-2}	Tilt 10^{-9} s^{-2}
12Z/18	470	296.0	0.059	13.1	23.1	4.5	1.2
00Z/19	552	296.9	0.069	14.0	25.4	-4.7	1.5
12Z/19	761	297.1	0.065	10.4	18.3	0.7	-3.4
13Z/19	764	297.1	0.065	8.4	14.8	5.3	-6.9
14Z/19	754	297.0	0.061	11.6	20.9	13.2	-9.8
15Z/19	714	298.5	0.053	15.1	31.5	-2.0	14.8
18Z/19	459	307.3	0.049	6.9	19.5	4.0	0.8

[8]Since computed PV gradients are so large in the frontal zone, even small non-conservative effects related to the interpolation procedure or inaccuracies in the trajectory computation may contribute to changes in the value of PV interpolated to the parcel position. The fourth-order spatial diffusion operator used in the model may also be acting to "dilute" parcel properties. Keyser and Pecnick (personal communication) observed similar behavior for trajectories computed within a two-dimensional primitive equation model of upper-level frontogenesis (Keyser and Pecnick, 1985).

5.3 Trajectory diagnostics for the cold conveyor belt

Trajectories 4 and 5 originate in the lower troposphere over the ocean to the north and east, respectively, of the surface low-pressure system and become incorporated into the storm circulation as shown in Fig. 13b. These trajectories are part of of the cold conveyor belt that originates in the lower troposphere within the strong anticyclone poised to the north and east of the developing storm system. Parcel 4 descends to the 994 mb level by 00Z/19, then turns toward the west, accelerates from 13 to 30 m s^{-1} between 06Z/19 and 10Z/19, and rises to the 850 mb level as it passes north of the storm center and curves around its western flank by 12Z/19. This parcel becomes involved in the developing low-level cyclonic circulation between 09Z/19 and 18Z/19, attaining an absolute vorticity value of 4.4 x 10^{-4} s^{-1} by 12Z/19. The parcel loops around the storm center during this period and is directed toward the east over the ocean during the last 6 h of the model simulation.

Table 3. Listing for cold conveyor belt parcel (trajectory 5 in Fig. 13b) for times listed in left-hand column. The variables include: pressure (p, mb), potential temperature (θ, K), specific humidity (q, g kg^{-1}), and vertical motion (ω, μb s^{-1}). Isobaric absolute vorticity, stretching, tilting terms, and potential vorticity as listed in Table 2.

COLD CONVEYOR BELT (TRAJECTORY 5)

Time	p mb	θ K	q g kg^{-1}	ω μb s^{-1}	$\zeta_p + f$ 10^{-5} s^{-1}	Stretch 10^{-9} s^{-2}	Tilt 10^{-9} s^{-2}	PV 10^{-6} K mb^{-1} s^{-1}
12Z/18	925	275.2	1.9	0.7	10.9	-0.3	0.7	2.5
00Z/19	970	280.9	5.0	0.6	4.4	-0.5	0.0	0.2
09Z/19	986	286.9	8.6	-1.7	2.7	-0.6	0.0	0.4
11Z/19	923	289.9	8.1	-21.2	28.3	71.7	0.2	14.8
12Z/19	778	294.4	5.0	-68.6	59.4	143.6	-6.8	21.2
18Z/19	381	302.8	0.1	-2.3	14.5	-6.5	0.5	2.2

Parcel 5 in Fig. 13b also originates within the cold anticyclonic circulation to the east of the developing storm system. As the parcel approaches the cyclone between 12Z/18 and 09Z/19, the potential temperature and mixing ratio increase by 11.7 K and 6.7 g kg^{-1} (Table 3), respectively, due to the heat and moisture fluxes in the ocean-influenced PBL. The parcel also begins to accelerate during the end of this period, with the

wind speed increasing from 12.0 to 26.0 m s^{-1} between 03Z/19 and 12Z/19 as the parcel enters the low-level jet southeast of the low-pressure center. As discussed by Whitaker et al. (1987), the isallobaric effects associated with the large SLP tendencies (see map insets in Fig. 6) make an important contribution to parcel accelerations during this period. Furthermore, the vertical displacement of the parcel that increases rapidly after 09Z/19 is also an important factor in the acceleration. The increasing ascent of the parcel after 09Z/19 (Table 3) within an environment in which the U_g changes with height can enhance the unbalanced nature of the flow, a factor which increases the magnitude of $|U|$ from 30 to 37 m s^{-1} in just 1 h [see Table 4 in Whitaker et al. (1987)]. As the parcel enters the region of strong ascent associated with the precipitation maximum and associated latent heat release north of the surface low (as indicated by increasing θ, decreasing q, and large negative values of ω after 09Z/19 in Table 3), it rapidly moves through the 700 to 850 mb layer and to the west of the closed low aloft. At this point, the parcel trajectory is directed toward higher heights. The parcel thus rapidly decelerates and turns to the right (Fig. 13b), marking the western boundary of the precipitation shield to the north and west of the simulated storm system, as indicated by the sharp gradients along the western edge of relative humidity maximum depicted in Fig. 5a. This pattern is also consistent with Eliassen and Kleinschmidt's description of the flow through a deepening cyclone (pp. 132-137) and with Carlson's (1980) schematic drawing of the relationship of the cold conveyor belt to the precipitation and cloud distribution to the north and west of an extratropical cyclone.

The vorticity diagnostics listed in Table 3 indicate that the cold conveyor belt is marked by a rapid increase in absolute vorticity due primarily to an increase in the stretching term of about an order of magnitude between 10Z/19 and 12Z/19. The stretching increases as the parcel begins to decelerate and rapidly rise through the 700 mb level. As the parcel rises above 700 mb into the region of maximum mass divergence aloft (Fig. 6c), the stretching term decreases to -6.5×10^{-8} s^{-2} and the absolute vorticity decreases as the parcel turns anticyclonically toward the east over New Jersey and Long Island (Fig. 13b).

5.4   Warm conveyor belt

Parcel 6 in Fig. 13b is chosen to represent the parcels which approach the developing cyclone from the south. These parcels begin at a higher pressure with higher values of θ and q than those in the cold conveyor belt discussed earlier. By 09Z/19, the parcel is accelerating toward the developing storm system in response to the increasing gradients in the SLP field (through the isallobaric wind) and also to the increasing ascent in a region where the geostrophic wind (i.e., the pressure gradient force) is changing with height (Whitaker et al., 1987). Sechrist and Dutton (1970) also emphasize the importance of the rapid acceleration of parcels approaching a coastal cyclone from the south and east (in conjunction with the increasing gradients in the SLP) and show that these accelerations are an important source of kinetic energy for the entire storm budget.

By 12Z/19, the wind speed has increased to near 30 m s^{-1} as the parcel ascends to the 700 mb level to a position just north of the developing surface low (Fig. 13b). The southern <u>origin</u> of the parcels that are located near the 700 mb level just north of the simulated surface low at 12Z/19 is identical to the trajectory results based on the radiosonde data described by Uccellini et al. (1985).

Table 4.   Listing for warm conveyor belt parcel (trajectory 6 in
           Fig. 13b) for times listed in left-hand column. Column
           headings and units listed in Table 3.

WARM CONVEYOR BELT (TRAJECTORY 6)

Time	p mb	θ K	q g kg^{-1}	ω μb s^{-1}	$\zeta_p + f$ 10^{-5} s^{-1}	Stretch 10^{-9} s^{-2}	Tilt 10^{-9} s^{-2}	PV 10^{-6} K mb^{-1} s^{-1}
12Z/18	1025	283.0	8.4	−0.2	7.3	0.3	0.0	2.7
00Z/19	1019	290.3	9.6	−0.4	5.4	0.8	0.8	1.7
09Z/19	960	289.4	9.3	−6.8	37.5	50.8	−1.7	15.0
11Z/19	854	292.5	6.7	−24.9	38.4	60.6	−8.1	14.3
1130Z/19	797	294.2	5.5	−38.9	47.1	66.8	22.9	15.9
12Z/19	706	297.1	3.9	−64.0	59.7	13.5	59.4	19.8
18Z/19	336	304.2	0.1	−1.8	2.6	−1.6	−4.5	2.6

The parcels in the warm conveyor belt are also marked by a concurrent increase in the potential vorticity and isobaric absolute vorticity between 09Z/19 and 12Z/19 (Table 4). The increase in the absolute vorticity is due

primarily to the stretching mechanism maximized below 700 mb. As the
parcel ascends above the 700 mb level, it passes through the region of
maximum mass divergence (Fig. 7d) and associated negative stretching,
resulting in a decrease in absolute vorticity after 12Z/19. The parcel
turns anticyclonically during this period and is directed northeastward and
then eastward off the New England coast by 21Z/19 (Fig. 13b).

The increase in PV to values greater than 10×10^{-6} K mb^{-1} s^{-1} near 09Z/19
(Table 4) occurs as this parcel passes through the low-level PV maximum
diagnosed within the coastal front/inverted trough (Section 3.3). The
increase of the PV <u>following</u> <u>a</u> <u>parcel</u> is related to diabatic processes
through the expression

$$\frac{d(PV)}{dt_\theta} = -(\zeta_\theta + f)\frac{\partial \dot{\theta}}{\partial p} + \frac{\partial \theta}{\partial p}\left[\underset{\sim}{\kappa} \cdot \left(\nabla_\theta \cdot \dot{\theta} \times \frac{\partial \underline{v}}{\partial \theta}\right)\right] , \qquad (3)$$

which neglects friction and where $\dot{\theta}$ is the diabatic heating rate dθ/dt. An
evaluation of the first term in eq. (3) for parcel 6 (Fig. 13b) between
1130Z/19 and 12Z/19 and the second term (transformed to p space) for the
2° x 2° box surrounding the storm center on the 700 mb level at 12Z/19
(Fig. 12d) indicates that the first term is nearly an order of magnitude
larger than the second term and accounts for nearly 70% of the PV increase
diagnosed with respect to parcel 6. Although there are difficulties in
making comparisons between these two terms, it appears from these results
that vertical gradients of the diabatic heating rate $\dot{\theta}$ (which is increasing
with increasing θ within the 1000 to 600 mb layer) in the region near and
above the inverted trough/coastal front would yield a net transport of mass
from a lower isentropic layer to the adjacent layer above, increasing the
stability in the lower isentropic layer and thus contributing to the
increase of the PV in the lower troposphere for the model simulation. At
the same time that PV is increased in the baroclinic region associated with
the coastal front, the increasing convergence experienced by the parcels as
they approach the developing storm acts to increase the absolute vorticity
for the parcels within the warm conveyor belt (Table 4).

6. SUMMARY AND CONCLUSIONS

A mesoscale model simulation is presented which captures the explosive development of the Presidents' Day cyclone on 19 February 1979. Output from the model is used to investigate the structure and evolution of a tropopause fold beneath the axis of an intensifying polar jet upwind of the region of incipient cyclogenesis. Vertical-transverse circulations beneath the jet core contribute to the intensifying frontal zone and the descent of dry stratospheric air, marked by high values of potential vorticity (PV). The path of this descending stratospheric air follows the PJ-trough system eastward to a position just west of the developing surface system by 09Z/19, as previously noted by Uccellini et al. (1985) using radiosonde and TOMS ozone data. By 12Z/19, the descending PV maximum merges with a low-level PV maximum associated with the developing coastal front/inverted trough. The explosive development phase of cyclogenesis coincides with the arrival of this dry, stratospheric air mass at low to mid levels in the cyclogenetic region and its merger with the low-level PV maximum.

The model simulation of the interaction between two separate PV maxima is consistent with the conceptual model described most recently by Hoskins et al. (1985). Through an "invertibility principle" first expressed by Kleinschmidt (1950), Hoskins et al. show that a positive PV anomaly in the upper troposphere will induce a cyclonic circulation which extends throughout the troposphere. Furthermore, a positive PV anomaly associated with a low-level baroclinic region will also induce a cyclonic circulation throughout the troposphere. This circulation can add to the circulation induced from the upper-level system, as long as the low-level anomaly remains downwind of the upper-level anomaly, maintaining a positive feedback between the two systems. The potential vorticity perspective discussed by Hoskins et al. is similar to the scenario for type B cyclogenesis described by Petterssen and Smebye (1971) which involves the advection of vorticity ahead of an upper-level trough over a low-level baroclinic region, which also occurs in the simulation of the Presidents' Day storm.

The model results presented here are in agreement with the growing body of evidence that shows the importance of the interactions of diabatic and dynamical processes throughout the depth of the troposphere which are important for explosively developing cyclones like the Presidents' Day storm. The Eulerian and Lagrangian model diagnostics reveal the following: (1) The cyclogenetic region is marked by the convergence of three major

airstreams. Cold, dry air which originates in the lower stratosphere and upper troposphere within the tropopause fold over the north-central United States descends toward the storm center from the southwest. Air which originates at low levels in the anticylonic flow associated with a strong surface high is moistened and warmed as it flows within the ocean-influenced PBL toward the storm system and then ascends and accelerates as it approaches the storm center from the east-southeast. These two airstreams correspond to the "dry airstream" and the "cold conveyor belt" in Carlson's (1980) conceptual model of airflow through mid-latitude cyclones, and their convergence coincides with the rapid spinup of the storm system and is responsible for the asymmetric cloud distribution observed in satellite imagery. A "warm conveyor belt" is also diagnosed for this simulated cyclone, although this airstream is not as pronounced as the other two. The southerly current accelerates toward the surface low, passes through the low-level PV maximum, ascends through the storm system, and then turns toward the northeast. (2) The vorticity of the parcels in the all of the airstreams is increased primarily by intense vertical stretching below the 700 mb level in the region where the various airstreams appear to converge. The production of vorticity by convergence (stretching) dominates in the lower troposphere with the vertical and horizontal vorticity advections acting to increase the vorticity in the middle troposphere. Strong positive vertical advection of vorticity in the 800 to 500 mb layer advects lower-tropospheric vorticity generated by convergence upward into the middle troposphere. This result is consistent with Johnson and Downey's (1975, 1976) diagnostic budget study of a rapidly developing cyclone based on angular momentum concepts. They show that the vertical transport of angular momentum, enhanced by latent heat release, is important for the development and maintenance of the mid-level vortex above the developing surface low. Positive differential vorticity advection above the surface low provides favorable quasi-geostrophic forcing during the period of explosive deepening. (3) The ascent and divergence of the airstreams north of the developing storm center are associated with a maximum layer of mass divergence that contributes to the continual deepening of the simulated surface low.

These model results indicate that the convergence of various airstreams that undergo important changes during the 24 h prior to cyclogenesis at distances ranging up to 2,000 km away from the storm center played a crucial role in the rapid spinup of the storm system. The convergence allowed for the realization of the high "potential" for a spinup

represented by the separate PV maxima in the upper and lower troposphere. Furthermore, the subsequent divergence of the airstreams is related to the increasing mass divergence above 700 mb, which contributes to the rapid deepening of the surface cyclone as measured by the decreasing SLP. Given the interaction among the various physical processes throughout the entire troposphere and lower stratosphere, attempts to isolate the relative importance of upper- and lower-tropospheric processes that combine to produce rapidly developing cyclones are not likely to be very meaningful, especially since these processes continually interact in a mutually beneficial manner as they contribute to the rapid development of the storm system.

7.   REFERENCES (for parts I and II)

Atlas, R., 1987: The role of oceanic fluxes and initial data on the numerical prediction of an intense coastal storm. Dynamics of Atmospheres and Oceans, 10, 359-388.

Bleck, R., 1973: Numerical forecasting experiments based on the conservation of potential vorticity on isentropic surfaces. J. Appl. Meteor., 12, 737-752.

_____, and C. Mattocks, 1984: A preliminary analysis of the role of potential vorticity in Alpine lee cyclogenesis. Beitr. Phys. Atmos., 57, 357-368.

Bjerknes, J., and J. Holmboe, 1944: On the theory of cyclones. J. Meteor., 1, 1-22.

Bosart, L. F., 1981: The Presidents' Day snowstorm of 18-19 February 1979: A subsynoptic-scale event. Mon. Wea. Rev., 109, 1542-1566.

_____, and S. C. Lin, 1984: A diagnostic analysis of the Presidents' Day storm of February 1979. Mon. Wea. Rev., 112, 2148-2177.

Cahir, J. J., 1971: Implications of circulations in the vicinity of jet streaks at subsynoptic scales. Ph.D. Thesis, Pennsylvania State University, 170 pp.

Carlson, T. N., 1980: Airflow through midlatitude cyclones. Mon. Wea. Rev., 108, 1498-1509.

Chou, S.-H., and D. Atlas, 1982: Satellite estimates of ocean-air heat fluxes during cold air outbreaks. Mon. Wea. Rev., 110, 1434-1450.

Cressman, G., 1959: An operational objective analysis scheme. Mon. Wea. Rev., 87, 367-374.

Danielsen, E. F., 1968: Stratospheric-tropospheric exchange based upon radioactivity, ozone and potential vorticity. J. Atmos. Sci., 25, 502-518.

_____, 1980: Stratospheric source for unexpectedly large values of ozone measured over the Pacific Ocean during GAMETAG, August, 1977. J. Geophys. Res., 85, 401-412.

Durst, C. S., and R. C. Sutcliffe, 1938: The importance of vertical motion in the development of tropical revolving storms. Quart. J. Roy. Meteor. Soc., 64, 75-84.

Eliassen, A., and E. Kleinschmidt, 1957: Dynamical meteorology. Handbuch der Physik, Vol. 48, J. Bartels, Ed., Springer-Verlag, 1-154.

Godson, W. L., 1950: A study of the derivation of wind speeds and directions from geostrophic values. Quart. J. Roy. Meteor. Soc., 76, 3-15.

Haltiner, J. G., and R. T. Williams, 1980: Numerical Prediction of Dynamic Meteorology. John Wiley and Sons, Inc., 477 pp.

Hoskins, B. J., M. E. McIntyre, and A. W. Robertson, 1985: On the use and significance of isentropic potential vorticity maps. Quart. J. Roy. Meteor. Soc., 111, 877-946.

Johnson, D. R., and W. K. Downey, 1975: The absolute angular momentum of storms: Quasi-Lagrangian diagnostics 2. Mon. Wea. Rev., 103, 1063-1076.

_____, and W. K. Downey, 1976: The absolute angular momentum budget of an extratropical cyclone: Quasi-Lagrangian diagnostics 3. Mon. Wea. Rev., 104, 3-14.

Kaplan, M. L., J. W. Zack, V. C. Wong, and J. J. Tuccillo, 1982: Initial results from a mesoscale atmospheric simulation system and comparisons with the AVE-SESAME I data set. Mon. Wea. Rev., 110, 1564-1590.

Keyser, D., and M. J. Pecnick, 1985: A two-dimensional primitive equation model of frontogenesis forced by confluence and horizontal shear. J. Atmos. Sci., 42, 1259-1282.

_____, and M. A. Shapiro, 1986: A review of the structure and
    dynamics of upper-level frontal zones. Mon. Wea. Rev., 114, 452-499.

_____, and L. W. Uccellini, 1987: Regional models: Emerging research
    tools for synoptic meteorologists. Bull. Amer. Meteor. Soc., 68,
    306-320.

Keyser, D. A., and D. R. Johnson, 1984: Effects of diabatic heating on the
    ageostrophic circulation of an upper tropospheric jet streak. Mon.
    Wea. Rev., 112, 1710-1724.

Kocin, P. J., and L. W. Uccellini, 1985a: A survey of major East Coast
    snowstorms, 1960-1983. Part 1: Summary of surface and upper-level
    characteristics. NASA TM 86195 [NTIS N85-27471], 101 pp. (Also
    tentatively accepted for publication as a Meteorological Monograph.)

_____, and L. W. Uccellini, 1985b: A survey of major East Coast
    snowstorms, 1960-1983. Part 2: Case studies of eighteen storms.
    NASA TM 86196 [NTIS N85-27272], 214 pp. (Also tentatively accepted
    for publication as a Meteorological Monograph.)

Kuo, H. L., 1974: Further studies of the parameterization of the influence
    of cumulus convection on large-scale flow. J. Atmos. Sci., 31,
    1232-1240.

Molinari, J., 1982: A method for calculating the effects of deep cumulus
    convection in numerical models. Mon. Wea. Rev., 110, 1527-1534.

Newton, C. W., and E. Palmen, 1963: Kinematic and thermal properties of a
    large-amplitude wave in the westerlies. Tellus, 15, 99-119.

Palmen, E., and C. W. Newton, 1969: Atmospheric Circulation Systems, Their
    Structure and Physical Interpretation. Int. Geophys. Ser., Vol. 13,
    Academic Press, 603 pp.

Petersen, R. A., 1986: Three-dimensional objective analysis using a
    detailed isentropic cross-sectional procedure. Mon. Wea. Rev., 114,
    719-735.

_____, J. J. Tuccillo, K. F. Brill, and L. W. Uccellini, 1985:
    The sensitivity of a mesoscale forecast model to detailed, three-
    dimensional isentropic initial analyses and varied vertial model
    resolution. Preprints, 7th Conf. on Numerical Weather Prediction,
    Amer. Meteor. Soc., Montreal, Canada, 83-90.

Petterssen, S., and S. J. Smebye, 1971: On the development of
    extratropical storms. Quart. J. Roy. Meteor. Soc., 97, 457-482.

Reed, R. J., 1955: A study of a characteristic type of upper-level
    frontogenesis. J. Meteor., 12, 226-237.

_____, and E. F. Danielsen, 1959: Fronts in the vicinity of the tropopause. Arch. Meteor. Geophys. Bioklim., A11, 1-17.

Sechrist, F. S., and J. A. Dutton, 1970: Energy conversions in a developing cyclone. Mon. Wea. Rev., 98, 354-362.

Shapiro, M. A., 1970: On the applicability of the geostrophic approximation to upper-level frontal motions. J. Atmos. Sci., 27, 408-420.

_____, 1975: Simulation of upper-level frontogenesis with a 20-level isentropic coordinate primitive equation model. Mon. Wea. Rev., 104, 591-604.

Sutcliffe, R. C., and A. G. Forsdyke, 1950: The theory and use of upper air thickness patterns in forecasting. Quart. J. Roy. Meteor. Soc., 76, 189-217.

Uccellini, L. W., and D. R. Johnson, 1979: The coupling of upper- and lower-tropospheric jet streaks and implications for the development of severe convective storms. Mon. Wea. Rev., 107, 682-703.

_____, P. J. Kocin, R. A. Petersen, C. H. Wash, and K. F. Brill, 1984: The Presidents' Day cyclone of 18-19 February 1979: Synoptic overview and analysis of the subtropical jet streak influencing the pre-cyclogenetic period. Mon. Wea. Rev., 112, 31-55.

_____, D. Keyser, K. F. Brill, and C. H. Wash, 1985: The Presidents' Day cyclone of 18-19 February 1979: Influence of upstream trough amplification and associated tropopause folding on rapid cyclogenesis. Mon. Wea. Rev., 113, 962-988.

_____, R. A. Petersen, K. F. Brill, P. J. Kocin, and J. J. Tuccillo, 1987: Synergistic interactions between an upper-level jet streak and diabatic processes that influence the development of a low-level jet and secondary cyclone. Mon. Wea. Rev. (September issue).

Whitaker, J. S., L. W. Uccellini, and K. F. Brill, 1987: A model-based diagnostic study of the explosive development phase of the Presidents' Day cyclone. Mon. Wea. Rev. (submitted).